

# In-Plane Optical Anisotropy of Layered Gallium Telluride

Shengxi Huang,<sup>†</sup> Yuki Tatsumi,<sup>‡</sup> Xi Ling,<sup>\*,†</sup> Huaihong Guo,<sup>§</sup> Ziqiang Wang,<sup>||</sup> Garrett Watson,<sup>⊥</sup> Alexander A. Puretzy,<sup>#</sup> David B. Geohegan,<sup>#</sup> Jing Kong,<sup>†</sup> Ju Li,<sup>||</sup> Teng Yang,<sup>∇,‡</sup> Riichiro Saito,<sup>‡</sup> and Mildred S. Dresselhaus<sup>\*,†,⊥</sup>

<sup>†</sup>Department of Electrical Engineering and Computer Science, Massachusetts Institute of Technology, Cambridge, Massachusetts 02139, United States

<sup>‡</sup>Department of Physics, Tohoku University, Sendai 980-8578, Japan

<sup>§</sup>College of Sciences, Liaoning Shihua University, Fushun 113001, China

<sup>||</sup>Department of Nuclear Science and Engineering, Massachusetts Institute of Technology, Cambridge, Massachusetts 02139, United States

<sup>⊥</sup>Department of Physics, Massachusetts Institute of Technology, Cambridge, Massachusetts 02139, United States

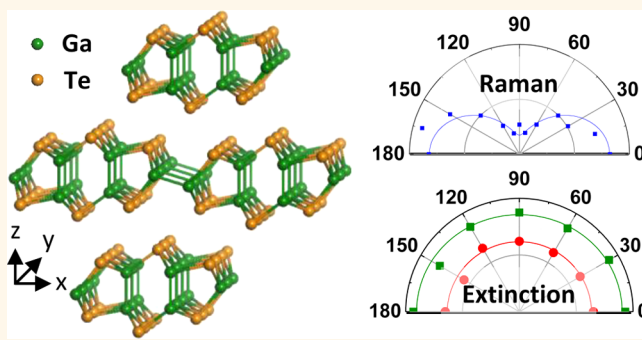
<sup>#</sup>Center for Nanophase Materials Sciences, Oak Ridge National Laboratory, Oak Ridge, Tennessee 37831, United States

<sup>∇</sup>Shenyang National Laboratory for Materials Science, Institute of Metal Research, Chinese Academy of Sciences, Shenyang 110016, China

## Supporting Information

**ABSTRACT:** Layered gallium telluride (GaTe) has attracted much attention recently, due to its extremely high photoresponsivity, short response time, and promising thermoelectric performance. Different from most commonly studied two-dimensional (2D) materials, GaTe has in-plane anisotropy and a low symmetry with the  $C_{2h}^3$  space group. Investigating the in-plane optical anisotropy, including the electron–photon and electron–phonon interactions of GaTe is essential in realizing its applications in optoelectronics and thermoelectrics. In this work, the anisotropic light-matter interactions in the low-symmetry material GaTe are studied using anisotropic optical extinction and Raman spectroscopies as probes. Our polarized optical extinction spectroscopy reveals the weak anisotropy in optical extinction spectra for visible light of multilayer GaTe. Polarized Raman spectroscopy proves to be sensitive to the crystalline orientation of GaTe, and shows the intricate dependences of Raman anisotropy on flake thickness, photon and phonon energies. Such intricate dependences can be explained by theoretical analyses employing first-principles calculations and group theory. These studies are a crucial step toward the applications of GaTe especially in optoelectronics and thermoelectrics, and provide a general methodology for the study of the anisotropy of light-matter interactions in 2D layered materials with in-plane anisotropy.

**KEYWORDS:** light-matter interaction, electron–photon interaction, polarization-dependent Raman spectroscopy, polarization-dependent optical extinction, group theory, optical transition selection rules



Two-dimensional (2D) materials constitute a large family with various members from the ones with high in-plane symmetry, such as graphene, to those with low in-plane symmetry, such as black phosphorus (BP), gallium telluride (GaTe), tin selenide (SnSe) and rhenium disulfide (ReS<sub>2</sub>).<sup>1–5</sup> These materials show diverse optical and electrical properties depending on their structures.<sup>6–11</sup> In particular, low-symmetry 2D materials show significant in-plane anisotropy in their electrical, optical and thermal properties. For example, compared to the  $D_{6h}$  symmetry of graphene, the reduced

symmetry ( $D_{2h}$ ) of BP has been reported to result in the mobility,<sup>12</sup> photoemission,<sup>8</sup> and thermoelectric ZT factor<sup>13,14</sup> being larger along the armchair direction than along the zigzag direction. In our recent research,<sup>15</sup> we used spectroscopic techniques to reveal the anisotropic light-matter interactions in

Received: July 26, 2016

Accepted: August 16, 2016

Published: August 16, 2016

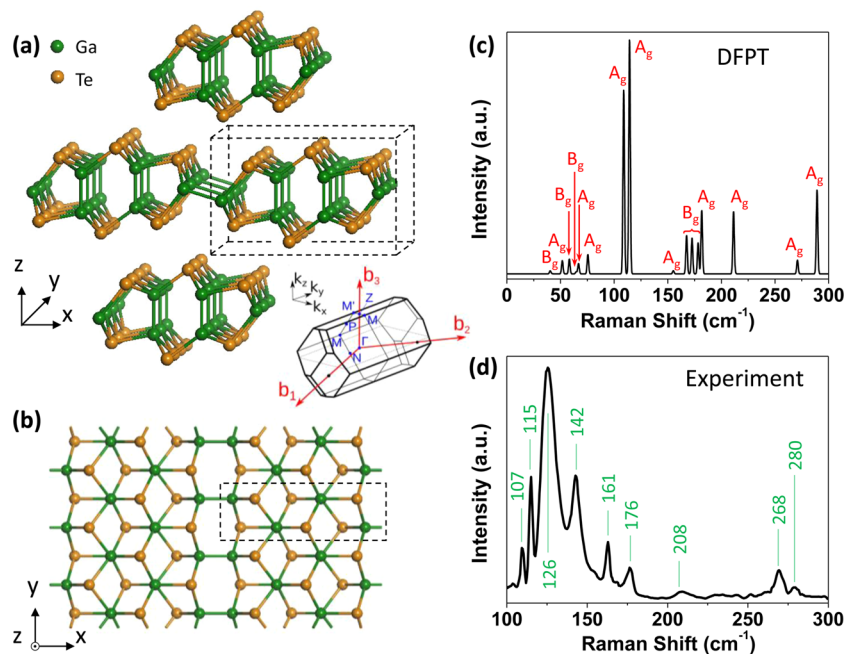


**Figure 1.** Crystal structure and Raman spectra of layered GaTe. (a) Front view for the crystal structure of bulk GaTe. (b) Top view for monolayer GaTe. The black dashed boxes in (a) and (b) correspond to the same group of atoms. Inset of (a): Brillouin zone for the primitive unit cell of bulk GaTe. (c) Calculated nonresonant Raman spectrum of bulk GaTe by DFPT methods. The symmetry of each mode is labeled. (d) Experimental Raman spectrum of a 125 nm thick GaTe flake at room temperature and under vacuum ( $10^{-5}$  mbar). The measurement was performed with 532 nm laser excitation. The peak frequencies are shown in units of  $\text{cm}^{-1}$ .

BP, including electron–photon and electron–phonon interactions, which indicates that it is crucial to understand the detailed anisotropy before applying the low-symmetry layered material to practical applications.<sup>6,10,12,16,17</sup>

As one of the important members among low-symmetry layered materials, GaTe has gained increasing attention in recent years.<sup>18–28</sup> With a direct bandgap of  $\sim 1.7$  eV for thicknesses ranging from few-layer to bulk, GaTe has demonstrated extremely high photoresponsivity ( $10^4$  A/W) and a short response time (6 ms) in photodetectors,<sup>20</sup> and also promising potentials in various other photonic applications such as solar cells, imaging arrays, radiation detectors, nonlinear optics,<sup>22,27,29</sup> as well as in thermoelectric devices.<sup>30,31</sup> Although the in-plane anisotropic performance of those properties has been observed,<sup>2,24,32</sup> the reason behind, as well as a convenient spectroscopic identification of the crystalline orientation, are still under exploration.

In this work, we report the in-plane optical anisotropy in the low-symmetry layered material GaTe, including its anisotropic optical absorption, optical extinction and Raman scattering, which reveal anisotropic light-matter interactions. We found that a GaTe multilayer shows a weak anisotropy of optical absorption and extinction in the visible spectral range, but Raman intensity shows a strong dependence on crystalline orientation. These experimental observations can be explained by first-principles calculations and group theory analyses. Moreover, due to the thickness dependence of the energy band structure and the symmetry of each energy level, the anisotropies of the Raman intensity show an intricate dependence on flake thickness, photon and phonon energies, which can be explained by group theory and optical transition selection rules. This work provides important guidelines for the design of optoelectronic and thermoelectric devices made of

GaTe, and presents a general methodology for the study of optical anisotropy in layered materials with in-plane anisotropy.

## RESULTS AND DISCUSSION

Bulk GaTe is a layered material with monoclinic structure as shown in Figure 1(a,b), which consists of 6 Ga and 6 Te atoms in the primitive unit cell. The adjacent GaTe layers are stacked to each other in the  $z$ -direction by van der Waals forces. Bulk GaTe has  $C_{2h}^3$  ( $C2/m$ ) symmetry,<sup>20,33,34</sup> which has a 2-fold rotational axis  $C_2$  ( $y$ -axis) and a mirror plane  $\sigma_h$  ( $x$ - $z$  plane). The inset in Figure 1(a) illustrates the Brillouin zone with several high-symmetry points  $\Gamma$ ,  $M$ ,  $Z$ ,  $M'$ ,  $P$  and  $N$ . According to our density functional theory (DFT) calculations (Figure S1), a direct bandgap is located at the  $Z$  point ( $E_g = 1.65$  eV) and slightly larger bandgaps can be seen at the  $P$  or  $M$  point ( $E_g = 1.80$  eV), which is consistent with the previous works.<sup>23,24</sup> Both the highest valence band and the lowest conduction band are almost flat along the  $M$ - $Z$ - $M'$ - $P$ - $M$  line of the Brillouin zone and optical transitions for energies close to the bandgap are expected to occur along this line.

The nonresonant Raman spectrum obtained from the density functional perturbation theory (DFPT) calculations is shown in Figure 1(c). According to group theory and the calculated phonon dispersion relation (Figure S2(a)), GaTe has 36 phonon modes in total, 18 of which are Raman-active: 12  $A_g$  modes and 6  $B_g$  modes. The calculated frequency values and vibrational motions of all the 36 phonon modes are listed in Table S1 and Figure S3, respectively. Most of the calculated Raman peaks were also observed in our experiments, as seen in Figure 1(d) for a Raman spectrum on a multilayer GaTe flake measured in vacuum. The Raman modes that were not observed in experiments have either weak intensity or low frequency ( $< 100 \text{ cm}^{-1}$ ), which is out of the detection range of conventional Raman spectrometers.

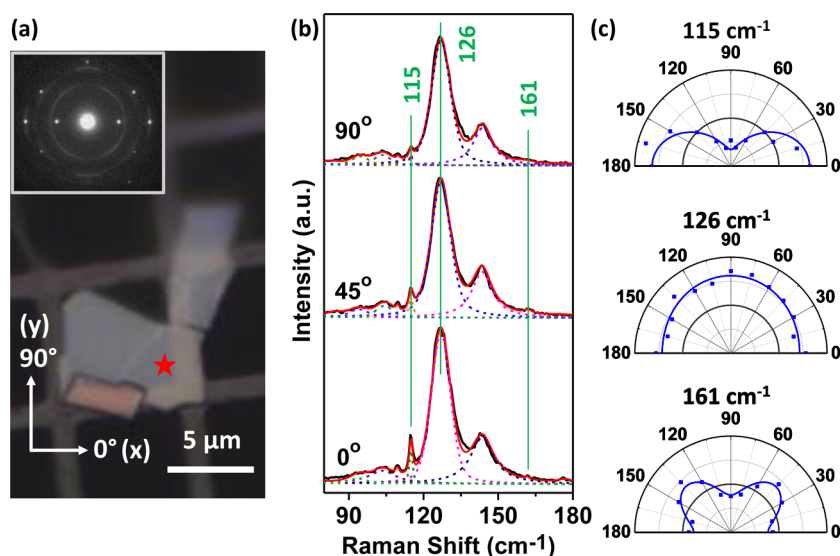


**Figure 2.** Polarized Raman spectra and diffraction pattern of a GaTe flake on a TEM grid. (a) The optical image of the GaTe flake on the TEM grid.  $0^\circ$  ( $90^\circ$ ) corresponds to  $x$ - ( $y$ -) axis of the GaTe crystal. The star indicates where the measurement was performed. Inset: The corresponding electron diffraction pattern. (b) Polarized Raman spectra of GaTe with polarization angles  $0^\circ$ ,  $45^\circ$  and  $90^\circ$ . (c) The Raman intensity vs polarization angle for three typical types of Raman modes:  $A_g$  mode ( $115\text{ cm}^{-1}$ ), double-resonant mode ( $126\text{ cm}^{-1}$ ) and  $B_g$  mode ( $161\text{ cm}^{-1}$ ); these three modes are also marked in (b). The squares are experimental values and the curves are numerical fittings. The Raman shift values are labeled above each panel. The excitation wavelength in (b,c) is  $633\text{ nm}$ .

To study the in-plane anisotropic optical properties, we carried out angle-resolved polarized Raman measurements. In Figure 2, the optical image (Figure 2(a)) of a GaTe flake on a TEM (transmission electron microscopy) grid is shown together with the corresponding TEM diffraction pattern (inset of Figure 2(a)) and the polarized Raman spectra (Figure 2(b)) with different polarization angles under parallel configuration. Raman spectra for additional polarization angles and peak fittings are shown in Figure S4. Eight Raman modes can be readily observed experimentally: 107, 115, 126, 142, 161, 208, 268, and  $280\text{ cm}^{-1}$ . From the electron diffraction pattern, the  $0^\circ$  axis corresponds to the  $x$ -axis of the crystalline orientation shown in Figure 1(a-b). According to the DFPT calculations, five Raman modes are  $A_g$  modes (107, 115, 208, 268,  $280\text{ cm}^{-1}$ ), one is  $B_g$  mode ( $161\text{ cm}^{-1}$ ), and two are double-resonant modes ( $126$ ,  $142\text{ cm}^{-1}$ ). These double-resonant modes<sup>35,36</sup> are created by two phonons of  $\sim 60\text{ cm}^{-1}$  and  $\sim 70\text{ cm}^{-1}$ , respectively, showing their broad features with Raman intensities proportional to the excitation laser power (Figure S2(b)). The shape of the phonon dispersion is flat and the phonon density of states is large around  $60\text{--}70\text{ cm}^{-1}$ , which is in good agreement with our observation that the Raman modes at 126 and  $142\text{ cm}^{-1}$  are strong.<sup>37,38</sup> Moreover, double-resonant modes generally have a weak anisotropy and exhibit broad features because many different combinations for two phonons are possible to contribute to Raman intensity (not necessarily just the  $\Gamma$  point phonons).

The polar plots of the angle-resolved polarized Raman intensity are summarized in Figure 2(c) for three typical Raman modes:  $A_g$  ( $115\text{ cm}^{-1}$ ), double-resonant ( $126\text{ cm}^{-1}$ ) and  $B_g$  ( $161\text{ cm}^{-1}$ ) modes, which are also marked in Figure 2(b). The polar plots of other modes are shown in Figure S5. It can be seen that Raman-active modes show a variety of degrees of anisotropy: under  $633\text{ nm}$  laser excitation, the double-resonant modes at 126 and  $142\text{ cm}^{-1}$  exhibit weak anisotropy, while the modes at 107, 115, 208, 268, and  $280\text{ cm}^{-1}$  show relatively stronger anisotropy with a period of  $180^\circ$  and with maximum

intensities along the  $x$ -axis.<sup>37</sup> This anisotropy supports the interpretation of the five modes with the same  $A_g$  symmetry. On the other hand, the mode around  $161\text{ cm}^{-1}$  shows a 4-fold anisotropy with a period of  $90^\circ$ , and the maximum (minimum) intensities along  $45^\circ$  and  $135^\circ$  (along the crystal axes  $x$  and  $y$ ). This further confirms the different symmetry ( $B_g$ ) of the  $161\text{ cm}^{-1}$  mode<sup>37</sup> compared to the five other modes with  $A_g$  symmetry. It can be seen that the crystalline orientation directly probed by TEM (inset of Figure 2(a)) is well matched with the polarized Raman profiles (Figures 2(c) and S5). These phenomena in GaTe show that polarized Raman spectroscopy can indicate crystalline orientation, and the anisotropy of the Raman intensity is strongly related to phonon symmetry. Similar phenomena have also been reported in other 2D materials with in-plane anisotropy.<sup>39,40</sup>

Furthermore, the detailed dependences of the in-plane anisotropy of the Raman intensity on different factors: flake thickness, excitation laser wavelength and phonon frequency, were all studied. In Table 1, we list the polar plots of the polarized Raman intensities under different excitation wavelengths (532, 633, and  $785\text{ nm}$ ) and with different flake thicknesses (58 and  $136\text{ nm}$ ) for first-order Raman modes at 107, 115, 161, 208, 268, and  $280\text{ cm}^{-1}$ . Table S2 shows the same information for double-resonant modes ( $126$ ,  $142\text{ cm}^{-1}$ ). The flakes used for the Raman measurements in Table 1 are mechanically exfoliated from a single-crystal bulk GaTe, and show variations in thicknesses but are physically connected that ensures the same crystalline orientation. In fact, we have measured more than 60 flakes, and found that the Raman profiles are maintained for thicknesses from 51 to  $68\text{ nm}$ , in which the  $58\text{ nm}$ -thickness is chosen as the representative for this thickness range. Similarly, the Raman profiles for the flake with a thickness of  $136\text{ nm}$  also represent the thickness range from 110 to  $170\text{ nm}$ . For few-layer flakes (thickness smaller than  $\sim 15\text{ nm}$ ), the Raman signals are very weak, partly due to the change of the atomic structure and the small light-matter interactions in those GaTe flakes.<sup>19,20</sup>

Table 1. Raman Anisotropy Dependence on Flake Thickness, Laser Wavelength and Phonon Frequency<sup>a</sup>

Laser Peak (cm <sup>-1</sup> )	532 nm		633 nm		785 nm	
	Thin (58 nm)	Thick (136 nm)	Thin	Thick	Thin	Thick
107						
115						
161					weak	
208	weak				weak	weak
268						
280					weak	weak

<sup>a</sup>The Raman intensity polar plots of two flakes with typical thicknesses: 58 and 136 nm, are shown here. These two flakes have the same crystalline orientation. The dots are experimental values and the curves are numerical fittings. The laser excitation wavelengths and the Raman frequencies are also labeled. 0° (90°) corresponds to *x*- (*y*-) axis of the GaTe crystal.

As seen in Table 1, the degree of anisotropy for the Raman modes depends not only on phonon mode symmetry, but also on phonon frequency (phonon energy), excitation laser wavelength (photon energy) and flake thickness. It can be seen from Table 1 that the major maximum of the Raman intensity is aligned along either 0° or 90° for all the Raman modes except for the 161 cm<sup>-1</sup> mode, and for all the excitation wavelengths used. This indicates that either 0° or 90° corresponds to the *x*-axis of the GaTe crystal. The Raman anisotropic profiles are observed to change with laser excitation wavelengths: the major maxima for 532 nm laser excitation are seen to be rotated by 90° from the major maxima for the 633 and 785 nm laser excitation for some Raman modes, such as the 107, 115, 208, and 268 cm<sup>-1</sup> modes. We also notice that the major maxima of the polarized Raman intensity remain along the same direction (along 0°) for all the *A<sub>g</sub>* modes measured under 633 and 785 nm laser excitations, but can change their directions to be either along 0° or 90° for 532 nm laser. According to the results in Figure 2, the major maxima for the Raman polar plots of the *A<sub>g</sub>* modes with 633 nm laser excitation correspond to the *x*-axis of the crystal. Therefore, in Table 1, 0° corresponds to the *x*-axis of the GaTe crystal. The two groups

of flake thicknesses presented here also show differences in the Raman profiles, which indicates the dependence of the anisotropic light-matter interactions on the flake thickness. From Table 1, we can see that the thin and thick flakes share the same major maxima direction (either at 0° or at 90°) for different Raman modes and excitation wavelengths. The Raman anisotropy dependence on flake thickness is reflected in the polar plot shape (or the degree of anisotropy): some modes show stronger anisotropy for the thick flakes than the thin flakes (such as 107, 115, 268, 280 cm<sup>-1</sup> modes under 532 nm laser), but some show similar degrees of anisotropy for both the thin and the thick flakes (such as 107 cm<sup>-1</sup> mode under 633 nm laser, and 115 cm<sup>-1</sup> mode under 785 nm laser), and some show stronger anisotropy for the thin flakes than the thick ones (such as 115 cm<sup>-1</sup> mode under 633 nm laser). This complexity in the degree of anisotropy can be explained by the optical transition selection rules, which will be described below. In addition, it can be seen that for some modes, secondary maxima appear, such as those at 0° for the 208 and 268 cm<sup>-1</sup> modes, and at 90° for the 280 cm<sup>-1</sup> mode measured under 532 nm (*E<sub>L</sub>* = 2.33 eV) laser excitation in the thick flakes. This observation is similar to the case of BP,<sup>15,40,41</sup> and suggests that the light



absorption, birefringence and phase difference in the Raman tensor elements are relevant for GaTe.<sup>40–42</sup> We can also see that the secondary maxima for the thick flakes are more pronounced than those measured for the thin ones for certain modes (268 and 280  $\text{cm}^{-1}$  under 532 nm laser). These observations further confirm that the secondary maxima are related to the optical absorption of GaTe and to the birefringence effect,<sup>15,40–42</sup> since the thicker flakes have larger absorption and the absorption coefficient of GaTe at 2.33 eV (532 nm) is larger than that at 1.96 eV (633 nm) and at 1.58 eV (785 nm). These effects will be explained below. The results presented in Table 1 provide a strong indication of the anisotropic Raman intensity in GaTe and its intricate dependence on phonon energy, photon energy and flake thickness, which offers useful guidelines for the applications of GaTe.

Besides Raman scattering, we further studied the optical absorption and optical extinction of GaTe flakes. The extinction is calculated as  $\ln(I_0/I)$ , where  $I$  and  $I_0$  are the light intensities transmitted through the quartz substrate on and off a GaTe flake, respectively. Since the origin of the extinction is optical absorption in GaTe, it is important to measure the anisotropy of optical extinction. Here we measured the extinction spectra in the wavelength range from 450 to 790 nm. The extinction for nonpolarized light increases with increasing flake thicknesses (Figure S6). For very thin GaTe flakes, such as the 6 nm-thick flake, almost no optical extinction is observed. The extinction of GaTe for polarized light was further investigated for the flakes on a quartz substrate shown in Figure 3(a). In order to determine the crystalline orientation of the flakes, we used the results of polarized Raman measurements on them (Figure S7), which indicated the 0° and 90° orientations in Figure 3(a) correspond to  $x$ - and  $y$ -axes, respectively.

The optical extinction spectra on the 112 nm-thick flake (labeled with a star in Figure 3(a)) for  $x$ - and  $y$ -polarized incident light are shown in Figure 3(b). It can be seen that the extinction for  $y$ -polarization is slightly smaller than for  $x$ -polarization, indicating that the optical extinction in multilayer GaTe shows weak anisotropy, despite the in-plane low symmetry and structural anisotropy of GaTe. The inset in Figure 3(b) shows a polar plot for the extinction of the 112 nm-thick flake at wavelengths of 532 and 633 nm ( $E_L = 2.33, 1.96$  eV, respectively) at different polarization angles, which also indicates the weak in-plane anisotropy of the optical extinction in the GaTe flake. More polarized extinction profiles for the other connected flakes (see Figure 3(a)) are shown in Figure S7(b–f), indicating weak extinction anisotropy, and slightly stronger optical extinction for the  $x$ -polarized light than for the  $y$ -polarized light as well. Such weak anisotropy in the optical extinction of GaTe is consistent with the previous work on bulk samples.<sup>2</sup> Figure 3(c) shows the thickness dependence of the ratio of the integrated extinctions in the visible range (450 to 790 nm) along the  $x$ - and  $y$ -directions, which indicates extinction anisotropy. It can be observed that the ratio is small for all the measured thicknesses (below 1.3), suggesting the weak anisotropy of the optical extinction in GaTe. In thin flakes (thickness smaller than  $\sim 40$  nm), the extinction ratio is relatively large and can reach  $\sim 1.3$ . The ratio drops as thickness increases and becomes close to 1.0 (isotropic) for the thickness range 50–130 nm. For even thicker flakes ( $>160$  nm), there is a rise of the extinction ratio and this rise is probably due to interference effect of light multireflected at the boundaries of

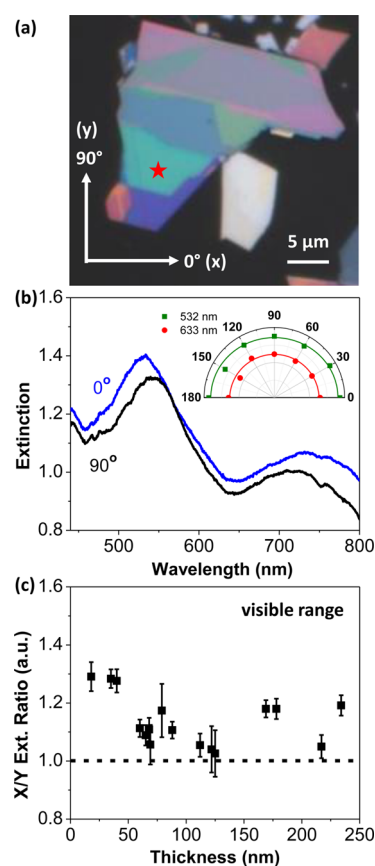


**Figure 3.** Experimental optical extinction of GaTe. (a) The optical microscope image of GaTe flakes on a quartz substrate. (b) Polarized optical extinction spectra measured with incident light polarized at 0° and 90° on the flake labeled with a star in (a). The flake thickness is 112 nm. The inset of (b) shows the extinction at wavelengths 532 and 633 nm with different polarization angles. The polarization angles correspond to the angular coordinates in (a). From the polarized Raman results shown in Figure S7(g,h), 0° and 90° correspond to  $x$ - and  $y$ -axes of the GaTe crystal, respectively. (c) Thickness dependence of the extinction ratio of  $x$ - and  $y$ -polarized light. The optical extinction is integrated in the visible spectral range from 450 to 790 nm. The dashed horizontal line indicates that the ratio equals 1.0 (isotropic).

quartz substrate and GaTe flake, which can play a role when the thickness of the flake is comparable to or larger than the wavelength of light but is negligible for thin flakes. The extinction ratios at the individual wavelengths 532, 633, and 785 nm are provided in Figure S8, which show the similar thickness evolution as in Figure 3(c). Some other anisotropic 2D materials, such as BP,<sup>15,43</sup> show stronger anisotropy in optical extinction than GaTe. The ratio of the integrated extinction of BP in the visible range can be 1.6 for a 225 nm-thick flake and 1.5 for a 9 nm-thick flake.<sup>15</sup> The relatively weak extinction anisotropy of GaTe is advantageous for its practical application in optoelectronic devices, in the sense that the device performance is not sensitive to the polarization angle of the incident light and thus does not require a strict crystalline orientation determination for general use. However, the flake thickness and the choice of substrate should be considered in the design of optoelectronic devices based on GaTe.

In order to explain the observed anisotropies of Raman scattering and optical extinction for GaTe, we carried out a calculation of the electron–photon interactions. The details of

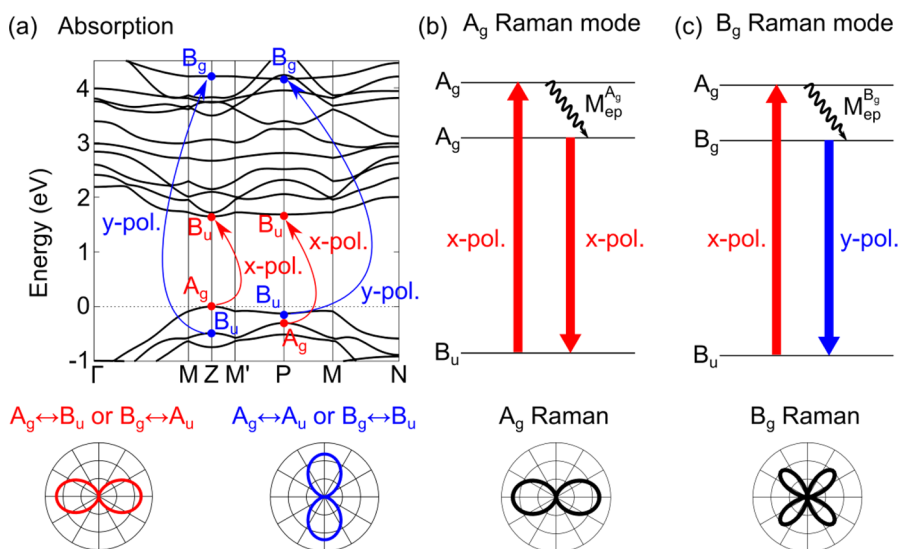


**Figure 4.** Optical transition selection rules in bulk GaTe. (a) Selection rules of optical transition near the Fermi energy at the  $P$  and  $Z$  points in the Brillouin zone, and the anisotropic optical absorption corresponding to the transitions activated by  $x$ -polarized (red arrows and curve) and  $y$ -polarized (blue arrows and curve) light. (b,c) One of the expected transitions for Raman scattering and polarization shape for the  $A_g$  (b) and  $B_g$  (c) modes at the  $Z$  or  $P$  point.  $M_{ep}^{A_g}$  ( $M_{ep}^{B_g}$ ) indicates the electron–phonon interaction emitting an  $A_g$  ( $B_g$ ) phonon. Red and blue arrows indicate the transition activated by  $x$ - and  $y$ -polarized light, respectively. In (a–c), the horizontal (vertical) axes in the polar plots correspond to  $x$ - ( $y$ -) axes.

the calculation can be found in Section 1 of [Supporting Information](#) (SI). Briefly, the optical absorption spectra can be obtained by calculating absorption coefficient  $\alpha$ . According to Fermi's Golden Rule,  $\alpha$  is proportional to the square of the electron–photon matrix element,  $\langle m|H_{op}|i\rangle$ ,<sup>44</sup> which describes the optical transition from the state  $i$  to  $m$ , and the matrix element is given by the inner product of the dipole vector  $\langle m|\nabla|i\rangle$  and the light polarization vector. When the polarization of the incident light changes, this inner product gives the polarization dependence of  $\alpha$ . On the other hand, when the state  $m$  or  $i$  changes by changing the flake thickness or the laser excitation wavelength, the matrix element  $\langle m|H_{op}|i\rangle$  and its polarization dependence change correspondingly. This result is known as the optical transition selection rules, and can be explained by group theory (details in Section 2 of SI). In the case of monoclinic bulk GaTe, the high symmetry points  $\Gamma$ ,  $Z$  and  $P$  in the Brillouin zone belong to the  $C_{2h}^3$  ( $C2/m$ ) space group. The symmetry of the eigenfunction for each energy band at the  $Z$  and  $P$  points (Figure S9) was determined by first-principles calculation. The  $Z$  and  $P$  points have the largest probability for optical transitions, and Figure 4(a) shows the selection rules of the optical transitions near the Fermi energy. The transitions between the  $A_g$  state and the  $B_u$  state and between the  $A_u$  state and the  $B_g$  state occur by  $x$ -polarized light, while the transitions between the  $A_g$  state and the  $A_u$  state and between the  $B_g$  state and the  $B_u$  state occur by  $y$ -polarized light. The main contribution near the gap energy ( $\lambda > 600$  nm) comes from  $x$ -polarized light, and as the photon energy increases, the  $y$ -polarized light is partially absorbed and the optical absorption/extinction anisotropy becomes weaker. This is due to the involvement of more energy bands in the absorption which contribute to different anisotropies as the photon energy increases. In line with the experimental results, the calculation also yields larger absorption for  $x$ - than for  $y$ -polarized light for the photon energy near the bandgap (Figure S10(a)).

With these selection rules of optical transitions and group theory, we can explain the intricate Raman polarization dependence presented in Table 1. The Raman intensity can be obtained by incorporating two electron–photon matrix elements with one electron–phonon matrix element as follows:

$$I_\nu(E_L) = \left| \sum_{i,m,m'} \frac{\langle f|H_{op}|m'\rangle \langle m'|H_{ep}^\nu|m\rangle \langle m|H_{op}|i\rangle}{(E_L - \Delta E_{mi})(E_L - \hbar\omega_\nu - \Delta E_{m'i})} \right|^2 \quad (1)$$

where  $\Delta E_{mi} = E_m - E_i - i\Gamma$ ,  $m$  ( $m'$ ) is the intermediate state and  $\Gamma$  is a broadening factor corresponding to the lifetime of photoexcited electrons. The initial ( $i$ ) and final ( $f$ ) states are the same in a Raman process. If we neglect the polarization dependence of the electron–phonon matrix element  $\langle m'|H_{ep}^\nu|m\rangle$ , the polarization dependence of the Raman intensity can be described by the product of two electron–photon matrix elements,  $\langle f|H_{op}|m'\rangle$  and  $\langle m|H_{op}|i\rangle$ . We show the detailed selection rules for the  $A_g$  and  $B_g$  Raman modes in Section 3 of SI, and an example of the transition corresponding to the  $A_g$  and  $B_g$  modes at the  $Z$  or  $P$  point in Figure 4(b,c). For the  $A_g$  mode, the  $m$  and  $m'$  states have the same symmetry, and the two electron–photon interaction matrix elements in eq 1 have the same polarization dependence that gives a  $180^\circ$  period in the polarization dependence; while for the  $B_g$  mode, the  $m$  and  $m'$  states have different symmetries, and the two matrix elements have the opposite polarization dependences, resulting in the  $90^\circ$  period of the  $B_g$  polarization profile, which is consistent with the experimental results shown in Table 1. Using the above analyses, we can explain the phenomena of major maximum axis flipping shown in Table 1: for Raman modes under 532 nm laser excitation, the major axis can flip between  $0^\circ$  and  $90^\circ$ , while 633 and 785 nm lasers do not induce such flipping of major axes. This is because 532 nm (2.33 eV) laser can excite the electrons to several energy bands with different symmetries, making a complicated polarization profile. Moreover, at low laser excitation energy, the Raman

modes are mostly  $x$ -polarized, while at higher laser excitation energy, the Raman modes polarized along the  $y$ -axis exist (Figure 4(a)), which is in a good agreement with the experimental observations in Table 1. The differences in the degree of anisotropy for different flake thicknesses (Table 1) are due to the change in the energy band structures with flake thickness. Besides, it is observed in Table 1 that under 532 nm laser, the  $280\text{ cm}^{-1}$  Raman mode has  $x$ -polarization, different from the other  $A_g$  modes with  $y$ -polarization. This is because the electronic states involved in the Raman process are related to the phonon energy. Therefore, it is possible that under 532 nm laser and for the  $280\text{ cm}^{-1}$  phonon,  $x$ -polarized electron–photon interactions dominate, while for the other  $A_g$  modes with different phonon energies, the electron–photon interactions with  $y$ -polarization are dominant.

Our optical transition selection rules using quantum mechanical model and group theory are essential for the analysis of the Raman anisotropy in GaTe. If we adopt the classical theory of the Raman tensor for the polarization dependence of the Raman intensity, the phonon modes with the same symmetry would have the same polarization dependence under the same excitation wavelength.<sup>45</sup> However, as can be observed from Table 1, under 532 nm laser excitation, the maximum intensity for the  $A_g$  mode at  $280\text{ cm}^{-1}$  is along the  $y$ -axis, while the other  $A_g$  modes at 107, 115, 208,  $268\text{ cm}^{-1}$  are polarized toward the  $x$ -axis, which suggests the necessity of using quantum theory for the Raman intensity (eq 1) for understanding the polarization dependence.<sup>45</sup> Since we notice that there is small discrepancy of anisotropy between theory and experiment, it is expected that the anisotropy of the electron–phonon interaction contributes to the anisotropy of the Raman intensity, which will be part of the future work. This method of characterizing the optical anisotropy of GaTe can be generalized to other 2D materials with in-plane anisotropy, which should be of significant importance for designing thermoelectric, electronic and photonic devices.

In addition, it is demonstrated through calculation (see Section 4 of SI for details) that the interference effect can affect the anisotropies in the optical absorption and extinction, but is not as important for the Raman anisotropy (Figures S11–S12).<sup>40,46–48</sup> For the optical absorption, the calculation involving the interference effect (Figure S11(b,c)) reduces the intrinsic absorption anisotropy, which is obtained solely by the electron–photon matrix elements. It suggests that the interference effect plays an important role in the optical absorption and extinction in GaTe, which is consistent with the experimental results. However, the experimentally observed anisotropy of the Raman intensity cannot be mainly attributed to the interference effect (Figure S12(b)), but is mostly due to the anisotropy of light-matter interactions.

On the basis of the theory we developed, it is expected that intricate in-plane anisotropy occurs in many low-symmetry 2D materials. Indeed, it has been reported that Raman spectroscopy shows polarization dependence on the crystalline orientation for various low-symmetry 2D materials, such as in BP, GaTe, ReSe<sub>2</sub>, ReS<sub>2</sub>, SnSe, *etc.*<sup>45</sup> The dependence is related to the symmetry of the material. For example, the major axis of Raman intensity polar plot is along either the zigzag or armchair directions for the  $A_g$  modes in BP with  $D_{2h}$  symmetry, while in ReSe<sub>2</sub> and ReS<sub>2</sub> which have  $P\bar{1}$  symmetry, the major axis can be along different lattice directions.<sup>49,50</sup> Furthermore, due to the complexity of Raman process, such a polarization dependence can vary with factors such as excitation laser

wavelength, flake thickness, phonon frequency, *etc.*<sup>15,41</sup> The anisotropy of optical absorption and extinction can also be observed in some anisotropic 2D materials, but the degree of anisotropy depends on the actual electronic energy bands of the material and may not be directly connected to the structural anisotropy of the material. For example, BP with higher structural symmetry  $D_{2h}$ , shows stronger anisotropy of the optical absorption in the visible range than GaTe, which has relatively lower structural symmetry  $C_{2h}$ .<sup>15</sup> By the same token, the mobility anisotropy may not be directly related to the structural anisotropy, but is more closely related to the energy band diagram.<sup>12</sup> More studies on the anisotropic optical and electronic properties of other in-plane anisotropic 2D materials are necessary for the future applications of such materials, to provide more guidance on particular choices of materials to use for particular applications.

## CONCLUSION

In summary, we performed an experiment/theory integrated investigation of the anisotropic optical extinction and Raman scattering in GaTe, which reveals insights into the role of anisotropy in light-matter interactions. The anisotropy of optical extinction is generally weak in the visible spectral range for multilayer GaTe, despite the in-plane structural anisotropy for GaTe. However, the anisotropy of the Raman intensity is strong and sensitively depends on excitation laser energy, phonon energy and GaTe thickness. This intricate dependence of the Raman scattering anisotropy on these different parameters stems from optical transition selection rules, as dictated by group theory. This work underscores the importance of understanding the anisotropic light-matter interactions in GaTe as well as other layered materials with low symmetry and in-plane anisotropy. This work also provides useful guidelines for the exploration of applications in electronic, optoelectronic and thermoelectric devices based on GaTe.

## METHODS

**Sample Preparation and Characterization.** GaTe flakes were mechanically exfoliated from a bulk single-crystal GaTe onto 300 nm SiO<sub>2</sub>/Si or quartz substrates. The thicknesses of the flakes were measured by atomic force microscopy (AFM). To transfer the GaTe flakes onto the TEM grid, we first exfoliated the GaTe flakes onto a PMMA thin film spin-coated on a Si substrate. The locations of the GaTe flakes were identified using an optical microscope, and a C-flat TEM grid was placed upside-down on the GaTe flake. Then the TEM grid was sealed in a drop of PMMA to fix the position, and the whole structure was immersed in acetone to remove PMMA, ending up with GaTe flakes lying flat and clean on the TEM grid. The TEM measurement was made using the facility of Joel 2011 TEM. The selected area electron diffraction (SAED) pattern of the sample as shown in the inset of Figure 2(a) was taken with a camera length of 15 cm.

**Raman Measurements.** Raman spectra were measured using a Horiba Jobin-Yvon HR800 system with three excitation lasers (532, 633, and 785 nm). A 100× objective was used to focus the laser beam on the sample with the spot size of approximately 1 μm. The laser power at the sample location was about 0.5 mW. In the polarization dependence measurements, parallel backscattering configuration was used with the capability of sample rotation. The Raman peak parameters were obtained by fitting the spectra with Lorentzian/Gaussian line shapes.

**Microextinction Measurements.** The extinction spectra were measured on GaTe flakes placed on 0.5 mm thick quartz substrates using a home-built microextinction setup operating in the transmission



mode. The white light source (EQ-99XFC, Energetiq) was coupled out with 25  $\mu\text{m}$  diameter optical fiber. The white light was focused on the sample surface with spot size  $\sim 1.5 \mu\text{m}$  using two microscope objectives: a 5 $\times$ -collimating objective, NA (numeric aperture) = 0.1, and a 100 $\times$ -long working distance objective, NA = 0.8 in an inverted microscope. The transmitted light was collected by a 50 $\times$ -objective (NA = 0.5) in an upright microscope coupled to the inverted microscope, and was analyzed by a spectrometer (Spectra Pro 2300i,  $f = 0.3 \text{ m}$ ) equipped with a CCD camera (Pixis 256BR, Princeton Instruments). The extinction was calculated as  $\ln(I_0/I)$ , where  $I$  and  $I_0$  are the light intensities transmitted through the quartz substrate on and off a GaTe flake, respectively. Here the extinction includes both optical absorption and reflection which is analyzed theoretically in SI. For the polarized microextinction measurements, the incident white light was linearly polarized using a Glan-Taylor polarizer.

**Theoretical Calculations.** The electronic band structure of GaTe was calculated within the DFT method as implemented in the Quantum Espresso package.<sup>51</sup> We used a generalized gradient approximation (GGA) with Perdew–Burke–Ernzerhof (PBE) functional. Norm-conserving pseudopotential was used.<sup>52</sup> The kinetic energy cutoff for wave functions was set at 50 Ry. The Monkhorst–Pack scheme with  $8 \times 8 \times 8$  mesh was used to sample k-points of the Brillouin zone of bulk GaTe. Atomic coordinates of bulk GaTe were determined from experimental results.<sup>53,54</sup> The phonon dispersion relation of GaTe was calculated based on density functional perturbation theory<sup>55</sup> and the nonresonant Raman intensities were calculated based on Placzek approximation as introduced by Lazzeri and Mauri.<sup>56</sup>

## ASSOCIATED CONTENT

### Supporting Information

The Supporting Information is available free of charge on the ACS Publications website at DOI: 10.1021/acsnano.6b05002.

Detailed calculation of electron–photon interactions, theory of optical transition selection rules and group theory, detailed calculation of interference effect, calculated energy band diagrams and phonon dispersion relation, more spectra and polar plots of experimental Raman scattering and optical extinction, all phonon modes of GaTe from DFPT calculation (PDF)

## AUTHOR INFORMATION

### Corresponding Authors

\*E-mail: xiling@mit.edu.

\*E-mail: millie@mgm.mit.edu.

### Author Contributions

S.H., X.L., J.K. and M.S.D. initiated the project and designed the experiments. S.H., X.L., G.W. and A.A.P. performed experimental measurements and analyzed the data. Y.T., H.G., T.Y. and R.S. performed the theoretical analysis. Z.W. and J.L. helped with TEM measurements.

### Notes

The authors declare no competing financial interest.

## ACKNOWLEDGMENTS

S.H., X.L. and M.S.D. at MIT acknowledge National Science Foundation grant 2DARE (EFRI-1542815) for financial support. J.K. acknowledges support from U.S. Army Research Office through the MIT Institute for Soldier Nanotechnologies, under award number 023674. Microextinction measurements were conducted at the Center for Nanophase Materials Sciences, which is a DOE Office of Science User Facility. R.S. acknowledges MEXT grant (No. 25107005). T.Y. and H.G. acknowledge the NSFC Grant (No. 51331006, U1537204) and

Liaoning Shihua University Grant (2016XJJ-044) for financial support. T.Y. acknowledges China Scholarship Council for financial support.

## REFERENCES

- (1) Ling, X.; Wang, H.; Huang, S.; Xia, F.; Dresselhaus, M. S. The Renaissance of Black Phosphorus. *Proc. Natl. Acad. Sci. U. S. A.* **2015**, *112*, 201416581.
- (2) Sánchez-Royo, J. F.; Segura, A.; Muñoz, V. Anisotropy of the refractive index and absorption coefficient in the layer plane of gallium telluride single crystals. *Phys. Status Solidi* **1995**, *151*, 257–265.
- (3) Lucovsky, G.; White, R. M. Optical-Phonon Anisotropies in Layered Crystals. *Nuovo Cim. B Ser. 11* **1977**, *38*, 290–300.
- (4) Taube, A.; Łapińska, A.; Judek, J.; Zdrojek, M. Temperature Dependence of Raman Shifts in Layered ReSe<sub>2</sub> and SnSe<sub>2</sub> Semiconductor Nanosheets. *Appl. Phys. Lett.* **2015**, *107*, 013105.
- (5) Chenet, D. A.; Aslan, O. B.; Huang, P. Y.; Fan, C.; van der Zande, A. M.; Heinz, T. F.; Hone, J. C. In-Plane Anisotropy in Mono- and Few-Layer ReS<sub>2</sub> Probed by Raman Spectroscopy and Scanning Transmission Electron Microscopy. *Nano Lett.* **2015**, *15*, 5667–5672.
- (6) Wang, H.; Wang, X.; Xia, F.; Wang, L.; Jiang, H.; Xia, Q.; Chin, M. L.; Dubey, M.; Han, S. Black Phosphorus Radio-Frequency Transistors. *Nano Lett.* **2014**, *14*, 6424–6429.
- (7) Low, T.; Rodin, A. S.; Carvalho, A.; Jiang, Y.; Wang, H.; Xia, F.; Castro Neto, A. H. Tunable Optical Properties of Multilayer Black Phosphorus Thin Films. *Phys. Rev. B: Condens. Matter Mater. Phys.* **2014**, *90*, 075434.
- (8) Wang, X.; Jones, A. M.; Seyler, K. L.; Tran, V.; Jia, Y.; Zhao, H.; Wang, H.; Yang, L.; Xu, X.; Xia, F. Highly Anisotropic and Robust Excitons in Monolayer Black Phosphorus. *Nat. Nanotechnol.* **2015**, *10*, 517–521.
- (9) Ho, C. H.; Huang, Y. S.; Tiong, K. K.; Liao, P. C. Absorption-Edge Anisotropy in ReS<sub>2</sub> and ReSe<sub>2</sub> Layered Semiconductors. *Phys. Rev. B: Condens. Matter Mater. Phys.* **1998**, *58*, 16130–16135.
- (10) Ho, C. H.; Huang, Y. S.; Tiong, K. K. In-Plane Anisotropy of the Optical and Electrical Properties of ReS<sub>2</sub> and ReSe<sub>2</sub> Layered Crystals. *J. Alloys Compd.* **2001**, *317–318*, 222–226.
- (11) Guo, R.; Wang, X.; Kuang, Y.; Huang, B. First-Principles Study of Anisotropic Thermoelectric Transport Properties of IV–VI Semiconductor Compounds SnSe and SnS. *Phys. Rev. B: Condens. Matter Mater. Phys.* **2015**, *92*, 115202.
- (12) Xia, F.; Wang, H.; Jia, Y. Rediscovering Black Phosphorus as an Anisotropic Layered Material for Optoelectronics and Electronics. *Nat. Commun.* **2014**, *5*, 4458.
- (13) Luo, Z.; Maassen, J.; Deng, Y.; Du, Y.; Garrelts, R. P.; Lundstrom, M. S.; Ye, P. D.; Xu, X. Anisotropic in-Plane Thermal Conductivity Observed in Few-Layer Black Phosphorus. *Nat. Commun.* **2015**, *6*, 8572.
- (14) Lee, S.; Yang, F.; Suh, J.; Yang, S.; Lee, Y.; Li, G.; Sung Choe, H.; Suslu, A.; Chen, Y.; Ko, C.; Park, J.; Liu, K.; Li, J.; Hippalgaonkar, K.; Urban, J. J.; Tongay, S.; Wu, J. Anisotropic in-Plane Thermal Conductivity of Black Phosphorus Nanoribbons at Temperatures Higher than 100 K. *Nat. Commun.* **2015**, *6*, 8573.
- (15) Ling, X.; Huang, S.; Hasdeo, E. H.; Liang, L.; Parkin, W. M.; Tatsumi, Y.; Nugraha, A. R. T.; Puzos, A. A.; Das, P. M.; Sumpter, B. G.; Geoghegan, D. B.; Kong, J.; Saito, R.; Drndic, M.; Meunier, V.; Dresselhaus, M. S. Anisotropic Electron-Photon and Electron-Phonon Interactions in Black Phosphorus. *Nano Lett.* **2016**, *16*, 2260–2267.
- (16) Xia, F.; Wang, H.; Xiao, D.; Dubey, M.; Ramasubramanian, A. Two-Dimensional Material Nanophotonics. *Nat. Photonics* **2014**, *8*, 899–907.
- (17) Liu, E.; Fu, Y.; Wang, Y.; Feng, Y.; Liu, H.; Wan, X.; Zhou, W.; Wang, B.; Shao, L.; Ho, C.-H.; Huang, Y.-S.; Cao, Z.; Wang, L.; Li, A.; Zeng, J.; Song, F.; Wang, X.; Shi, Y.; Yuan, H.; Hwang, H. Y.; et al. Integrated Digital Inverters Based on Two-Dimensional Anisotropic ReS<sub>2</sub> Field-Effect Transistors. *Nat. Commun.* **2015**, *6*, 6991.
- (18) Zólyomi, V.; Drummond, N. D.; Fal'ko, V. I. Band Structure and Optical Transitions in Atomic Layers of Hexagonal Gallium



Chalcogenides. *Phys. Rev. B: Condens. Matter Mater. Phys.* **2013**, *87*, 195403.

(19) Hu, P.; Zhang, J.; Yoon, M.; Qiao, X.-F.; Zhang, X.; Feng, W.; Tan, P.; Zheng, W.; Liu, J.; Wang, X.; Idrobo, J. C.; Geohegan, D. B.; Xiao, K. Highly Sensitive Phototransistors Based on Two-Dimensional GaTe Nanosheets with Direct Bandgap. *Nano Res.* **2014**, *7*, 694–703.

(20) Liu, F.; Shimotani, H.; Shang, H.; Kanagasekaran, T.; Zólyomi, V.; Drummond, N.; Fal'ko, V. I.; Tanigaki, K. High-Sensitivity Photodetectors Based on Multilayer GaTe Flakes. *ACS Nano* **2014**, *8*, 752–760.

(21) Balitskii, O. A.; Jaeckel, B.; Jaegermann, W. Surface Properties of GaTe Single Crystals. *Phys. Lett. A* **2008**, *372*, 3303–3306.

(22) Bose, D. N.; Pal, S. Photoconductivity, Low-Temperature Conductivity, and Magnetoresistance Studies on the Layered Semiconductor GaTe. *Phys. Rev. B: Condens. Matter Mater. Phys.* **2001**, *63*, 235321.

(23) Sánchez-Royo, J. F.; Pellicer-Porres, J.; Segura, A.; Muñoz-Sanjosé, V.; Tobias, G.; Ordejón, P.; Canadell, E.; Huttel, Y. Angle-Resolved Photoemission Study and First-Principles Calculation of the Electronic Structure of GaTe. *Phys. Rev. B: Condens. Matter Mater. Phys.* **2002**, *65*, 115201.

(24) Yamamoto, A.; Syouji, A.; Goto, T.; Kulatov, E.; Ohno, K.; Kawazoe, Y.; Uchida, K.; Miura, N. Excitons and Band Structure of Highly Anisotropic GaTe Single Crystals. *Phys. Rev. B: Condens. Matter Mater. Phys.* **2001**, *64*, 035210.

(25) Fonseca, J. J.; Tongay, S.; Topsakal, M.; Chew, A. R.; Lin, A. J.; Ko, C.; Luce, A. V.; Salleo, A.; Wu, J.; Dubon, O. D. Bandgap Restructuring of the Layered Semiconductor Gallium Telluride in Air. *Adv. Mater.* **2016**, *28*, 6465.

(26) Shenoy, U. S.; Gupta, U.; Narang, D. S.; Late, D. J.; Waghmare, U. V.; Rao, C. N. R. Electronic Structure and Properties of Layered Gallium Telluride. *Chem. Phys. Lett.* **2016**, *651*, 148–154.

(27) Susoma, J.; Karvonen, L.; Säynätjoki, A.; Mehravar, S.; Norwood, R. A.; Peyghambarian, N.; Kieu, K.; Lipsanen, H.; Riikonen, J. Second and Third Harmonic Generation in Few-Layer Gallium Telluride Characterized by Multiphoton Microscopy. *Appl. Phys. Lett.* **2016**, *108*, 073103.

(28) Zhao, Q.; Wang, T.; Miao, Y.; Ma, F.; Xie, Y.; Ma, X.; Gu, Y.; Li, J.; He, J.; Chen, B.; Xi, S.; Xu, L.; Zhen, H.; Yin, Z.; Li, J.; Ren, J.; Jie, W. Thickness-Induced Structural Phase Transformation of Layered Gallium Telluride. *Phys. Chem. Chem. Phys.* **2016**, *18*, 18719–18726.

(29) Mandal, K. C.; Krishna, R. M.; Hayes, T. C.; Muzykov, P. G.; Das, S.; Sudarshan, T. S. Layered GaTe Crystals for Radiation Detectors. In *IEEE Nuclear Science Symposium & Medical Imaging Conference*; IEEE, 2010; pp 3719–3724.

(30) Rahmlow, T. D.; DePoy, D. M.; Fourspring, P. M.; Ehsani, H.; Lazo-Wasem, J. E.; Gratrix, E. J. Development of Front Surface, Spectral Control Filters with Greater Temperature Stability for Thermophotovoltaic Energy Conversion. In *AIP Conference Proceedings*; AIP, 2007; Vol. 890, pp 59–67.

(31) Pal, S.; Bose, D. Growth, Characterisation and Electrical Anisotropy in Layered Chalcogenides GaTe and InTe. *Solid State Commun.* **1996**, *97*, 725–729.

(32) Gousskov, L.; Gousskov, A. Resistivity Anisotropy in the Layer Plane of GaTe. *Phys. Status Solidi* **1979**, *51*, K213–K215.

(33) Pearson, W. B. The Crystal Structures of Semiconductors and a General Valence Rule. *Acta Crystallogr.* **1964**, *17*, 1–15.

(34) Camassel, J.; Merle, P.; Mathieu, H. Excitonic Absorption Edge of GaTe. *Physica B+C* **1980**, *99*, 309–313.

(35) Guo, H.; Yang, T.; Yamamoto, M.; Zhou, L.; Ishikawa, R.; Ueno, K.; Tsukagoshi, K.; Zhang, Z.; Dresselhaus, M. S.; Saito, R. Double Resonance Raman Modes in Monolayer and Few-Layer MoTe<sub>2</sub>. *Phys. Rev. B: Condens. Matter Mater. Phys.* **2015**, *91*, 205415.

(36) Venezuela, P.; Lazzeri, M.; Mauri, F. Theory of Double-Resonant Raman Spectra in Graphene: Intensity and Line Shape of Defect-Induced and Two-Phonon Bands. *Phys. Rev. B: Condens. Matter Mater. Phys.* **2011**, *84*, 035433.

(37) Irwin, J. C.; Clayman, B. P.; Mead, D. G. Long-Wavelength Phonons in GaTe. *Phys. Rev. B: Condens. Matter Mater. Phys.* **1979**, *19*, 2099–2105.

(38) Cerdeira, F.; Meneses, E. A.; Gousskov, A. Splittings and Correlations between the Long-Wavelength Optical Phonons in the Layer Compounds GaSe, GaTe, and GaSe<sub>1-x</sub>Te<sub>x</sub>. *Phys. Rev. B* **1977**, *16*, 1648–1654.

(39) Wu, J.; Mao, N.; Xie, L.; Xu, H.; Zhang, J. Identifying the Crystalline Orientation of Black Phosphorus Using Angle-Resolved Polarized Raman Spectroscopy. *Angew. Chem.* **2015**, *127*, 2396–2399.

(40) Mao, N.; Wu, J.; Han, B.; Lin, J.; Tong, L.; Zhang, J. Birefringence-Directed Raman Selection Rules in 2D Black Phosphorus Crystals. *Small* **2016**, *12*, 2627–2633.

(41) Ribeiro, H. B.; Pimenta, M. A.; de Matos, C. J. S.; Moreira, R. L.; Rodin, A. S.; Zapata, J. D.; de Souza, E. A. T.; Castro Neto, A. H. Unusual Angular Dependence of the Raman Response in Black Phosphorus. *ACS Nano* **2015**, *9*, 4270–4276.

(42) Kranert, C.; Sturm, C.; Schmidt-Grund, R.; Grundmann, M. Raman Tensor Formalism for Optically Anisotropic Crystals. *Phys. Rev. Lett.* **2016**, *116*, 127401.

(43) Qiao, J.; Kong, X.; Hu, Z.-X.; Yang, F.; Ji, W. High-Mobility Transport Anisotropy and Linear Dichroism in Few-Layer Black Phosphorus. *Nat. Commun.* **2014**, *5*, 4475.

(44) Sakurai, J. J.; Napolitano, J. J. *Modern Quantum Mechanics*, 2nd ed.; Addison-Wesley, 2011.

(45) Saito, R.; Tatsumi, Y.; Huang, S.; Ling, X.; Dresselhaus, M. S. Raman Spectroscopy of Transition Metal Dichalcogenides. *J. Phys.: Condens. Matter* **2016**, *28*, 353002.

(46) Li, S.-L.; Miyazaki, H.; Song, H.; Kuramochi, H.; Nakaharai, S.; Tsukagoshi, K. Quantitative Raman Spectrum and Reliable Thickness Identification for Atomic Layers on Insulating Substrates. *ACS Nano* **2012**, *6*, 7381–7388.

(47) Yoon, D.; Moon, H.; Son, Y.-W.; Choi, J. S.; Park, B. H.; Cha, Y. H.; Kim, Y. D.; Cheong, H. Interference Effect on Raman Spectrum of Graphene on SiO<sub>2</sub>/Si. *Phys. Rev. B: Condens. Matter Mater. Phys.* **2009**, *80*, 125422.

(48) Wang, Y. Y.; Ni, Z. H.; Shen, Z. X.; Wang, H. M.; Wu, Y. H. Interference Enhancement of Raman Signal of Graphene. *Appl. Phys. Lett.* **2008**, *92*, 043121.

(49) Zhao, H.; Wu, J.; Zhong, H.; Guo, Q.; Wang, X.; Xia, F.; Yang, L.; Tan, P.; Wang, H. Interlayer Interactions in Anisotropic Atomically Thin Rhenium Diselenide. *Nano Res.* **2015**, *8*, 3651–3661.

(50) He, R.; Yan, J.-A.; Yin, Z.; Ye, Z.; Ye, G.; Cheng, J.; Li, J.; Lui, C. H. Coupling and Stacking Order of ReS<sub>2</sub> Atomic Layers Revealed by Ultralow-Frequency Raman Spectroscopy. *Nano Lett.* **2016**, *16*, 1404.

(51) Giannozzi, P.; Baroni, S.; Bonini, N.; Calandra, M.; Car, R.; Cavazzoni, C.; Ceresoli, D.; Chiarotti, G. L.; Cococcioni, M.; Dabo, I.; Dal Corso, A.; de Gironcoli, S.; Fabris, S.; Fratesi, G.; Gebauer, R.; Gerstmann, U.; Gougoussis, C.; Kokalj, A.; Lazzeri, M.; Martin-Samos, L.; et al. QUANTUM ESPRESSO: A Modular and Open-Source Software Project for Quantum Simulations of Materials. *J. Phys.: Condens. Matter* **2009**, *21*, 395502.

(52) Hartwigsen, C.; Goedecker, S.; Hutter, J. Relativistic Separable Dual-Space Gaussian Pseudopotentials from H to Rn. *Phys. Rev. B: Condens. Matter Mater. Phys.* **1998**, *58*, 3641–3662.

(53) Alapini, F.; Flahaut, J.; Guittard, M.; Jaulmes, S.; Julien-Pouzol, M. Systeme Gallium-Tellure. *J. Solid State Chem.* **1979**, *28*, 309–319.

(54) HU, S.-Z.; PARTHÉ, E. Inorganic Crystal Structure Data to Be Presented in a Form More Useful for Further Studies. *Chin. J. Struct. Chem.* **2004**, *23*, 1150.

(55) Baroni, S.; de Gironcoli, S.; Dal Corso, A. Phonons and Related Crystal Properties from Density-Functional Perturbation Theory. *Rev. Mod. Phys.* **2001**, *73*, 515–562.

(56) Lazzeri, M.; Mauri, F. First-Principles Calculation of Vibrational Raman Spectra in Large Systems: Signature of Small Rings in Crystalline SiO<sub>2</sub>. *Phys. Rev. Lett.* **2003**, *90*, 036401.